Direct numerical simulation of a 30R long turbulent pipe flow at Re_τ = 3008

Junsun Ahn, Jae Hwa Lee, Jin Lee, et al.

View Online   Export Citation   CrossMark

ARTICLES YOU MAY BE INTERESTED IN

Direct numerical simulation of turbulent channel flow up to $Re_\tau = 590$
Physics of Fluids **11**, 943 (1999); https://doi.org/10.1063/1.869966

Wall-bounded turbulent flows at high Reynolds numbers: Recent advances and key issues
Physics of Fluids **22**, 065103 (2010); https://doi.org/10.1063/1.3453711

Hairpin vortex organization in wall turbulence
Physics of Fluids **19**, 041301 (2007); https://doi.org/10.1063/1.2717527

Physics of Fluids

Special Topic: Paint and Coating Physics

Submit Today!

AIP Publishing

Direct numerical simulation of a 30R long turbulent pipe flow at $Re_\tau = 3008$

Junsun Ahn,[1] Jae Hwa Lee,[2] Jin Lee,[1] Ji-hoon Kang,[3] and Hyung Jin Sung[1,a)]

[1]*Department of Mechanical Engineering, KAIST, 291 Daehak-ro, Yuseong-gu, Daejeon 305-701, South Korea*
[2]*School of Mechanical and Nuclear Engineering, UNIST, 50 UNIST-gil, Ulsan 689-798, South Korea*
[3]*Supercomputing Center, KISTI, 245 Daehak-ro, Yuseong-gu, Daejeon 305-806, South Korea*

A direct numerical simulation of a turbulent pipe flow at a high Reynolds number of $Re_\tau = 3008$ over a long axial domain length (30R) was performed. The streamwise mean velocity followed the power law in the overlap region ($y^+ = 90$–300; $y/R = 0.03$–0.1) based on the power law indicator function. The scale separation of the Reynolds shear stresses into two components of small- and large-scale motions (LSMs) revealed that the LSMs in the outer region played an important role in constructing the constant-stress layer and the mean velocity. In the pre-multiplied energy spectra of the streamwise velocity fluctuations, the bimodal distribution was observed at both short and long wavelengths. The k_x^{-1} region associated with the attached eddies appeared in $\lambda_x/R = 2$–5 and $\lambda_x/y = 18$–160 at $y^+ = 90$–300, where the power law was established in the same region. The k_z^{-1} region also appeared in $\lambda_z/R = 0.3$–0.6 at $y^+ = 3$ and 150. Linear growth of small-scale energy to large-scale energy induced the k_x^{-1} region at high Reynolds numbers, resulting in a large population of the LSMs. This result supported the origin of very-large-scale motions in the pseudo-streamwise alignment of the LSMs. In the pre-multiplied energy spectra of the Reynolds shear stress, the bimodal distribution was observed without the k_x^{-1} region. © 2015 AIP Publishing LLC. [http://dx.doi.org/10.1063/1.4922612]

I. INTRODUCTION

Scientific technical advancements have enabled us to reliably measure flow velocity profiles at high Reynolds numbers of up to $Re_\tau \approx 10^5$ in experimental turbulent pipe flows.[1] Many direct numerical simulations (DNSs) of turbulent pipe flows have been performed, although the Reynolds numbers in these simulations have been limited to $Re_\tau = O(10^3)$ due to the massive computational power and cost. Wu and Moin[2] performed a DNS of turbulent pipe flows at $Re_\tau = 1142$ with a streamwise domain length of 15R, where R is the pipe radius. Chin *et al.*[3] performed a DNS at $Re_\tau = 2003$ with 3πR. Hoyas and Jiménez[4] carried out a DNS of turbulent channel flows at the same Reynolds number ($Re_\tau = 2003$) with $8\pi h$, where h is the half-channel height. Recently, Lee and Moser[5] performed a DNS of turbulent channel flows ($Re_\tau = 5186$) with the same domain length ($8\pi h$). Since Monty *et al.*[6] and Lee and Sung[7] described the existence of very long meandering structures up to $O(30R)$, domains at least 8πR in length are required to capture the large- and very-large-scale motions (LSMs and VLSMs).

The streamwise mean velocity profile has been found to scale with the inner variables in the inner region and with the outer variables in the outer region. The validation of the mean velocity

---

a)Author to whom correspondence should be addressed. Electronic mail: hjsung@kaist.ac.kr. Tel.: 82-42-350-3027. Fax: 82-42-350-5027.

was limited to the spatial resolutions of flow field, because the indicators of the mean velocity were determined by the spatial derivatives along the wall-normal direction. The inner scaling variables are the friction velocity (u_τ) and the viscous length scale (ν/u_τ), where ν is the fluid kinematic viscosity. The outer scaling variables are the flow thickness (R, h, or δ), but the appropriate velocity scale is the same as that used in the inner region. These two scales led to the most famous logarithmic law (log law) in the overlap region, $U^+ = \kappa^{-1}\log(y^+) + B$, where κ is the von Kármán constant, B is the additive constant, y is the wall-normal distance, and the superscript $+$ indicates the inner scaling. Most experimental and numerical studies of wall-bounded turbulent flows have documented a log law over a wide range of Reynolds numbers;[8,9] however, turbulent pipe flows do not always follow the log law in the mean velocity. Wu and Moin[2] showed a power law in the mean velocity ($Re_\tau = 1142$), defined as $U^+ = Cy^{+\gamma}$, where C is the proportionality constant and γ is the power constant. Chin *et al.*[3] reported that the log law did not apply up to $Re_\tau = 2003$. In experiments ($Re_\tau > 5000$), McKeon *et al.*[10] observed both power and log laws, depending on y^+: the power law was observed over $50 < y^+ < 300$ and the log law was observed over $600 < y^+ < 0.12Re_\tau$. At extremely high Reynolds numbers, however, turbulent pipe flows were found to converge to the log law.[1,9] Experimental studies have revealed that the log law applies in pipe flow as well as channel flow at $Re_\tau = 1000$–3000.[11,12] Nagib and Chauhan[8] found that the constants in the log law changed, depending on the flow geometry, i.e., the log law applied but it was not universal. These distinct laws that conflicted in the overlap region motivated us to simulate a high-Reynolds-number turbulent pipe flow in the present study.

As the Reynolds number was increased up to $Re_\tau \approx 2000$, the outer regions of the pre-multiplied streamwise energy spectra of the streamwise velocity fluctuations became prominent.[13] Long-wavelength outer-scaled energy at long wavelength was created by contributions from the VLSMs, which modulated the near-wall small-scale motions (SSMs).[14,15] Kim and Adrian[16] first observed the existence of VLSMs based on the bimodal distribution in the energy spectra. Rosenberg *et al.*[17] observed traces of short and long wavelength peaks in turbulent pipe flows over a range of Reynolds numbers. Note that the presence of the long wavelength peak in the experimental studies was suspected to correspond to an artifact of Taylor's hypothesis.[18] Recent DNSs of turbulent channel flows at $Re_\tau = 5186$ revealed a clear outer region with $\lambda_x/\delta = 2\pi$,[5] similar to the regions observed in the turbulent boundary layer (TBL).[13] This finding contradicted the previous findings, which revealed that the long wavelength peaks in the pipe and channel flows were much longer than those present in the TBL.[11] A plateau, called the k_x^{-1} region, was observed in the pre-multiplied energy spectra and was attributed to the attached eddy hypothesis.[19,20] Nickels *et al.*[21] observed the k_x^{-1} region in TBL at $Re_\tau = 14\,380$. Rosenberg *et al.*[17] found the k_x^{-1} region at $Re_\tau = 3334$ in an experiment involving turbulent pipe flows. Lee and Moser[5] and del Álamo and Jiménez[18] revealed the k_x^{-1} region in the turbulent channel flow at $Re_\tau = 2003$ and $Re_\tau = 5186$, respectively; however, Morrison *et al.*[22] could not identify the k_x^{-1} region in the turbulent pipe flows at other Reynolds numbers ($Re_\tau = 1500$ and $100\,000$). Unlike the energy spectra corresponding to the streamwise velocity fluctuations, the energy spectra of the Reynolds shear stresses have not been extensively studied. The only attached variables (e.g., the streamwise velocity fluctuations) had the k_x^{-1} region in the energy spectra, but the detached ones (e.g., the Reynolds shear stress) did not have the k_x^{-1} region.[23]

The present study examined a DNS of a turbulent pipe flow at $Re_\tau = 3008$ to explore the issues raised among high Reynolds number flows. The axial domain length was 30R, long enough to capture the LSMs and VLSMs. The DNS data were compared with previous experimental and numerical data for validation. The power law of the streamwise mean velocity in the overlap region was evaluated based on the indicator function. The contributions of the LSMs and SSMs to the mean velocity and the Reynolds shear stress were measured. The pre-multiplied energy spectra of the streamwise velocity fluctuations and the Reynolds shear stress were analyzed. The presence of the bi-modal distribution and the k_x^{-1} and k_z^{-1} regions were examined and the scale growth of the LSMs and VLSMs was discussed. The quadrant analysis of the Reynolds shear stress was performed from the energy spectra to explain the statistical behavior of the turbulence structures.

II. NUMERICAL DETAILS

The Navier-Stokes and continuity equations in cylindrical coordinates were employed to describe an incompressible and fully developed turbulent pipe flow 30R in length. Here, r, z, and θ denote the radial, axial, and azimuthal directions, and u_r, u_z, and u_θ denote the corresponding velocity components. The centerline velocity (U_c) and the pipe radius (R) were used to non-dimensionalize the equations. The governing equations were temporally discretized using the Crank-Nicolson scheme and were spatially resolved using the second-order central difference scheme with a staggered grid. The velocity and pressure were decoupled using the fully implicit fractional step method.[24] No-slip conditions at the wall and periodic boundary conditions along the streamwise and azimuthal directions were employed. For convenience and for comparison with other geometries, the cylindrical coordinates were transformed to Cartesian coordinates: the streamwise direction, $x = z$; the wall-normal direction, $y = 1 - r$; the spanwise direction, $z = r\theta$, and the corresponding velocity components were $u = u_z$, $v = -u_r$, and $w = u_\theta$.[7,25] The velocity fluctuations were denoted using the prime symbol (e.g., u'), and the time- and spatial-averaged quantities of the mean velocity and the velocity fluctuations were expressed using a capital letter or bracket (e.g., U or $\langle u'u' \rangle$). A detailed description of the numerical simulation method may be found in Lee and Sung[7] and Ahn *et al.*[15]

The Reynolds number, calculated based on the pipe diameter (D) and the bulk velocity (U_b), was Re_D ($\equiv DU_b/\nu$) = 133 000, and the Kármán number was $Re_\tau = 3008$, the highest Reynolds number used in a DNS of a turbulent pipe flow. The statistics were averaged over sampling times of $600R/U_c$, which allowed a particle to travel 10 times down the length of the axial domain with the bulk velocity flow. The numbers of the grids and the spatial and temporal resolutions are summarized in Table I. The total number of grid points exceeded 30×10^9, and the raw data obtained from the three-direction velocities and pressures at each step used around 1 TB storage. We introduced a hybrid technique, which was a combination of OpenMP (Open Multi-Processing) and MPI (Message Passing Interface), to enhance the computational performance and to handle the massive memory. The simulations were performed using 4906 parallel cores (Intel Xeon X5570 2.93 GHz) in the KISTI Supercomputing Center.

A. Validation

The temporal history of the streamwise velocity fluctuations is displayed in Fig. 1(a). Two specific wall-normal positions of $y^+ = 15$ and 214 (=3.9$(Re_\tau)^{1/2}$) were chosen as representative points in the near-wall and overlap regions in which the maximum turbulent production and the log layer were found, respectively.[14] The profiles revealed turbulent velocity signals, and the interaction between the inner and outer regions was displayed. Fig. 1(b) presents the averaged streamwise Reynolds stress for the sampling time t_{avg}, $\langle \bullet \rangle = \int_{t_{ref}}^{t_{ref}+t_{avg}} \bullet dt$. Similarly, Fig. 1(c) presents the averaged streamwise energy spectra (Φ) of the streamwise and spanwise velocity fluctuations at $y^+ = 15$. The reference time t_{ref} was determined after the transient state. Since the statistics collapsed well after $t_{avg}^+ = 8164$, the present averaging time $600R/U_c$ ($t_{avg}^+ = 40\,820$) was enough for convergence.

Fig. 2(a) shows the profiles of the streamwise mean velocities in the turbulent pipe flows. The DNS data[2] obtained at $Re_\tau = 1142$ and the experimental data[1,11,12] obtained at $Re_\tau \approx 3000$ are included for comparison. The general trend of our profile was similar to that observed in other data. The profiles of the Reynolds stresses are shown in Fig. 2(b), based on the same previous data. The profiles agreed well with those reported by Wu and Moin[2] near the wall. The magnitude of the near-wall peak in the streamwise component exceeded that reported by Wu and Moin[2] as

TABLE I. Numerical parameters used in the present simulation.

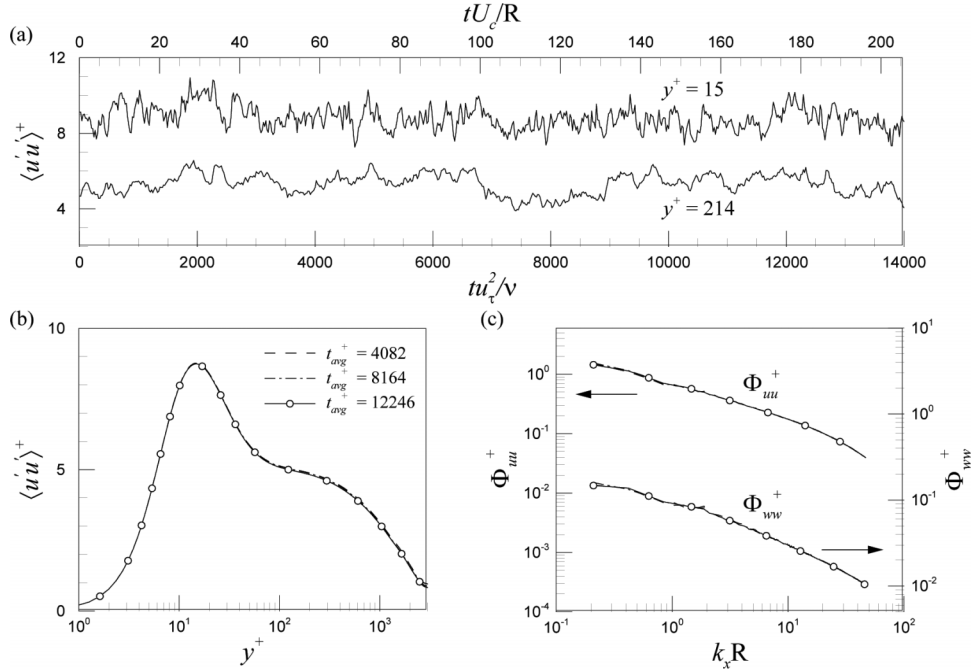| Re_D	Re_τ	(N_x, N_r, N_z)	Δx^+	Δr^+_{min}	Δr^+_{max}	$\Delta(R\theta)^+$	$\Delta t U_c/R$
133 000	3008	(12 289, 901, 3073)	7.34	0.36	9.91	6.15	0.003

FIG. 1. (a) Temporal history of the streamwise velocity fluctuations at $y^+ = 15$ and 214, (b) streamwise Reynolds stress, and (c) streamwise energy spectra of the streamwise and spanwise velocity fluctuations at $y^+ = 15$.

resulting from the effects of a high Reynolds number. The experimental data were collected using different spatial resolutions of hot-wires ($l^+ = l u_\tau / \nu$, where l is the hot-wire length): $l^+ = 30$[11] and 22[12]. These parameters nearly satisfied the criteria for an inner-scaled hot-wire spatial resolution.[26] Although these parameters satisfied the criteria, hot-wires with $l^+ = 22$ produced an attenuation in the streamwise Reynolds stress.[27] Although Hultmark *et al.*[1] employed a sufficient spatial resolution ($l^+ = 3.1$), the near-wall behaviors were slightly overestimated, possibly because of $l/d < 200$, where d is the diameter of a hot-wire,[26] or due to the insufficient temporal resolution.[1]

III. RESULTS

A. Mean velocity

1. Power law

A magnified view of the streamwise mean velocity through the buffer and overlap regions $y^+ = 10$–1000 is shown in Fig. 3 with the power and log laws,
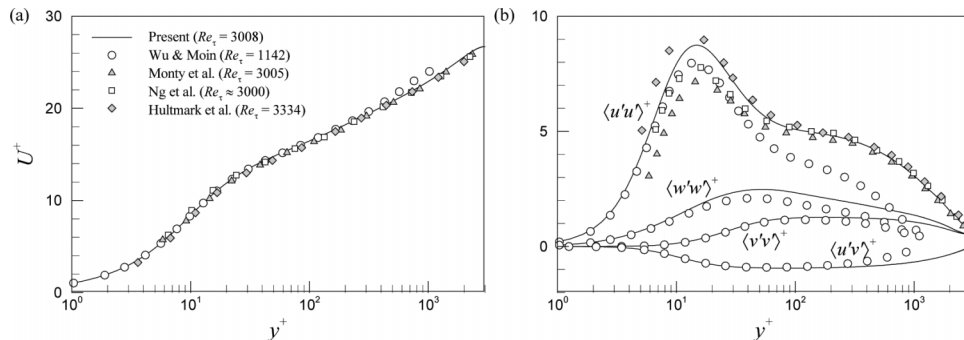

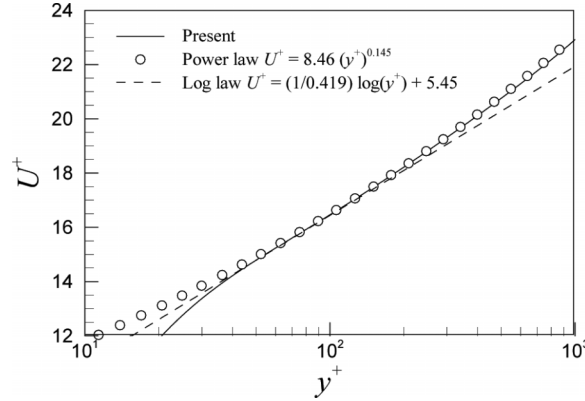FIG. 2. (a) Profiles of the streamwise mean velocity and (b) profiles of the Reynolds stresses.

FIG. 3. Scaling of the mean streamwise velocity by the power and log laws in the overlap region.

$$U^+ = C y^{+\gamma} : \text{power law,} \tag{1}$$

$$U^+ = (1/\kappa) \log(y^+) + B : \text{log law.} \tag{2}$$

The power law followed the mean velocity in the range $y^+ = 60$–600 ($y/R = 0.02$–0.2), whereas the profile matched the log law only over the range $y^+ = 40$–150 ($y/R = 0.013$–0.05), both within a 0.5% tolerance. Note that the log law region proposed by Marusic *et al.*[9] was 164 ($=3(Re_\tau)^{1/2}$) < $y^+ < 451$ ($=0.15Re_\tau$) at $1.8 \times 10^4 < Re_\tau < 6.3 \times 10^5$, slightly higher than ours due to the different Reynolds numbers. The power law coefficients ($C = 8.46, \gamma = 0.145$) were almost the same as reported values ($C = 8.48, \gamma = 0.142$ at $Re_\tau > 5000$),[10] indicating that the coefficients were independent of the Reynolds numbers. The power law in the present pipe flow at $Re_\tau = 3008$ indicated that the viscous effects of the wall remained in the overlap region.

The power and log laws were evaluated by each indicator function according to

$$\Gamma = \frac{y^+}{U^+} \frac{\partial U^+}{\partial y^+} = \gamma : \text{power law indicator function,} \tag{3}$$

$$\Xi = y^+ \frac{\partial U^+}{\partial y^+} = \frac{1}{\kappa} : \text{log law indicator function.} \tag{4}$$

Fig. 4 shows the profiles of the indicator functions, including the DNS data obtained at $Re_\tau = 934$,[15] for comparison. Fig. 4(a) shows that the profiles obtained at two Reynolds numbers were similar up to $y^+ \approx 100$. The profile corresponding to $Re_\tau = 3008$ reached a plateau ($\gamma = 0.145$) over the range $y^+ \approx 90$–300 ($y/R = 0.1$). The profiles of the log law indicator function shown in Fig. 4(b) exhibited qualitatively consistent behaviors up to $y^+ \approx 60$ with a local minimum of 2.387 ($=1/\kappa, \kappa = 0.419$).[10] Unlike the power law indicator function, no flat regions were observed within the overlap region for the log law indicator function, as shown in Fig. 4(b). The absence
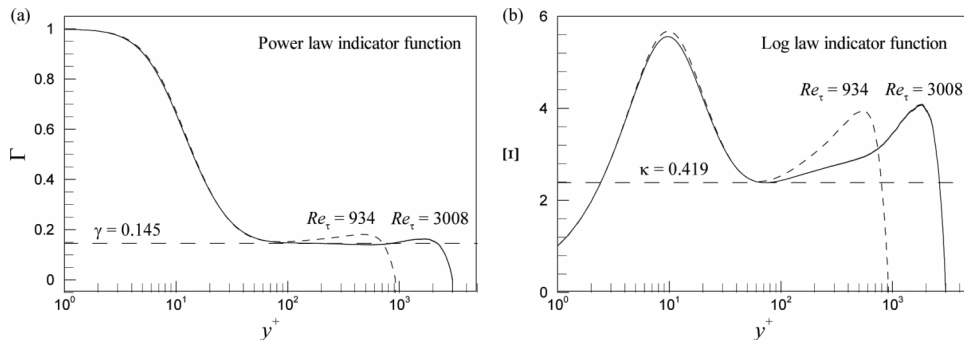

FIG. 4. Wall-normal distributions of the (a) power law and (b) log law indicator functions.

of a flat region has been observed in previous DNS studies.[2,3] The power law was located at $y^+ \approx 90$–300 ($y/R = 0.03$–0.1) in the inertial layer, which was similar to the experimental data of McKeon *et al.*[10] at similar Reynolds numbers. However, the present power law in the inertial layer was different from the previous sequential alignment of the power and log laws.[10] The previous power law was located at $y^+ = 50$–300, which was no longer in the inertial layer at higher Reynolds numbers ($Re_\tau \geq 5000$).[10] The power law indicator function provided clear evidence that the present mean velocity followed a power law in the overlap region at the present Reynolds number ($Re_\tau = 3008$). Note that previous numerical and experimental studies of turbulent channel flows at $Re_\tau \approx 900$–3000 reported the presence of a log law in the mean velocity, although a clear plateau was not observed in the log law indicator function.[4,11,12] A recent DNS of turbulent channel flows revealed a plateau ($\kappa = 0.384$) over the range $y^+ = 300$–780, in supportive of the log law at $Re_\tau = 5186$.[5]

2. Constant-stress layer

The constant-stress layer indicated that the Reynolds shear stress was independent of the distance from the wall.[19] The scale separation of the Reynolds shear stress was made to see the contribution of the two components of SSMs and LSMs to the constant-stress layer. Chin *et al.*[28] proposed a cut-off wavelength $\lambda_x^+ = 3000$ to demarcate the LSMs from the SSMs, and they showed that the contributions of the SSMs to the Reynolds shear stress were independent of the Reynolds number. Here, the LSMs encompassed the VLSMs, i.e., LSMs = LSMs + VLSMs. We found that the variation of the scale-separated Reynolds shear stress against the Reynolds numbers was small when the cut-off wavelength was larger than 3000 ($\lambda_x^+ \geq 3000$). We applied the same procedure as Chin *et al.*[28] to the DNS data of pipe flow ($Re_\tau = 934$ and 3008),[15] as shown in Fig. 5(a). The SSMs were similar, regardless of the Reynolds numbers, whereas the LSMs increased in the outer region along with the Reynolds number. This implied that the LSMs were more responsible for the maintenance of the constant-stress layer than the SSMs. The Reynolds shear stress was distributed across $y^+ = 50$–140 within a 1% tolerance of the maximum (0.941 65), similar to the log law region described in Sec. III A 1. If the Reynolds number was increased further, the LSMs became more active and the constant-stress layer followed a log law.

The scale separation of the Reynolds shear stress in a pipe flow at $Re_\tau = 934$[15] was compared with that in a channel flow at $Re_\tau = 930$ (Ref. 29) in Fig. 5(b). The contribution of the LSMs to the Reynolds shear stress was larger in the channel flow than in the pipe flow, even though the total Reynolds shear stresses were nearly equivalent. Note that the contributions of the SSMs in the outer region differed from the contributions of the LSMs toward the total Reynolds shear stresses in both flows. As shown in Fig. 5(b), the magnitude of the Reynolds shear stress associated with the LSMs in the core region of the pipe flow was smaller than the magnitude in the channel flow ($y^+ = 50$–930).
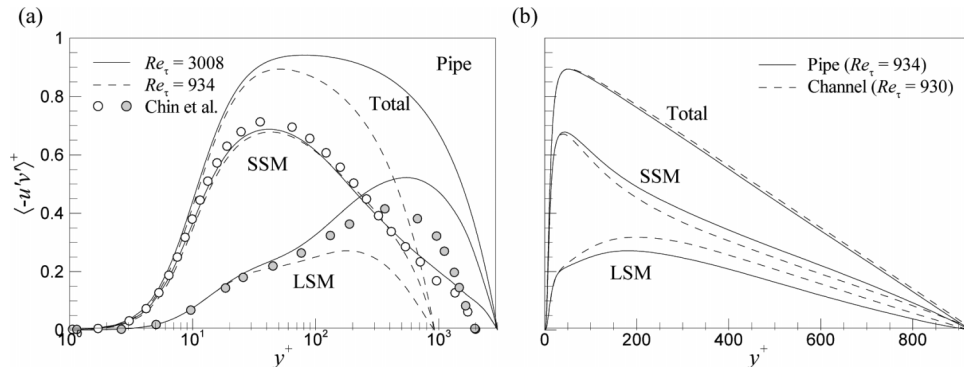

FIG. 5. Scale separation of the Reynolds shear stress. (a) Turbulent pipe flows at $Re_\tau = 3008$ and 934. (b) Turbulent pipe and channel flows at $Re_\tau \approx 930$. The white and grey circle symbols indicate the profiles of, respectively, the SSMs and LSMs.[28]
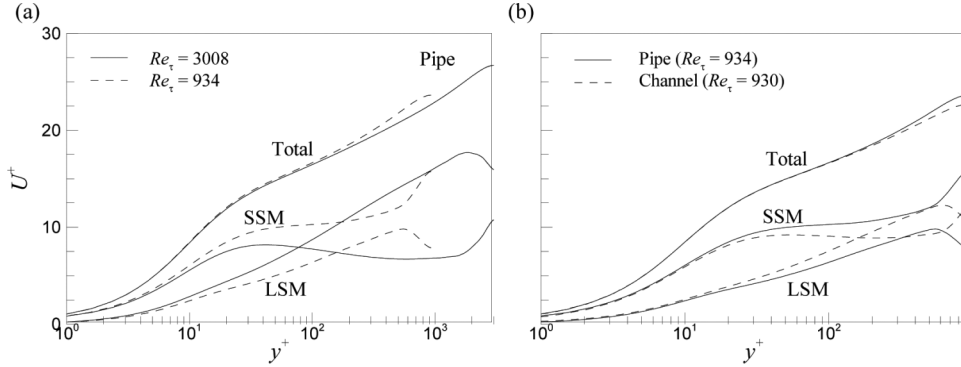
FIG. 6. Scale separation of the streamwise mean velocity. (a) Turbulent pipe flows at $Re_\tau = 3008$ and 934, (b) turbulent pipe and channel flows at $Re_\tau \approx 930$.

The scale separation of the streamwise mean velocity at $Re_\tau = 934$ and 3008 is shown in Fig. 6. The fractions of the LSMs and the SSMs in the streamwise Reynolds stress were employed to obtain the scale separation of the mean velocity,

$$U = U_{\mathrm{LSM}} + U_{SSM} = \frac{\langle u'u' \rangle_{\mathrm{LSM}}}{\langle u'u' \rangle} U + \frac{\langle u'u' \rangle_{\mathrm{SSM}}}{\langle u'u' \rangle} U, \qquad (5)$$

where $\langle u'u' \rangle_{\mathrm{LSM}} = \int_{\lambda_x^+ = 3000}^{\infty} \Phi_{uu}(\lambda_x)\mathrm{d}\lambda_x$ and $\langle u'u' \rangle_{\mathrm{SSM}} = \int_0^{\lambda_x^+ = 3000} \Phi_{uu}(\lambda_x)\mathrm{d}\lambda_x$. For $Re_\tau = 934$, the contribution of the LSMs was smaller than that of the SSMs in the entire wall-normal region. For $Re_\tau = 3008$, the contribution of the LSMs was larger than that of the SSMs at $y^+ > 70$. Fig. 6(b) showed different behaviors between pipe and channel flows even at the same Reynolds numbers. In the channel flow, the contribution of the SSMs was larger than that of the LSMs at $y^+ < 160$, and vice versa at $y^+ > 160$. This implied that the LSMs were more responsible for the growth of the mean velocity in the overlap region than the SSMs. In sum, since the LSMs in the pipe flow decayed more rapidly than in the channel flow due to space limitations in the core region, the LSMs in the pipe flow were more restricted than those in the channel flow. Lee *et al.*[30] found that the survival time of the LSMs was shorter in the pipe flow than in the channel flow. The different behaviors resulted from different geometries, i.e., different contributions of the LSMs in the pipe and channel flows. The structural differences between the pipe and channel flows probably resulted in different power and log laws that applied in the overlap region. These results supported the hypothesis[31] that LSMs were important contributions to a universal scaling law applicable in the overlap region if the volume fraction of large-scale structures was significant. Because the LSMs were more highly populated in the channel flow than in the pipe flow,[30] the highly active LSMs in the channel flow contributed to the mean velocity log law to a greater extent than they did in the pipe flow.

B. Energy spectra

1. Energy spectra of the streamwise velocity fluctuations

The one-dimensional (1-D) pre-multiplied streamwise energy spectra of the streamwise velocity fluctuations ($k_x\Phi_{uu}^+$) for $y/R < 0.1$ ($y^+ = 300$) and $y/R \geq 0.1$ are shown in Figs. 7(a) and 7(b), respectively, along with previously reported experimental data collected at similar Reynolds numbers. The intensities of the energy spectra near the wall ($y^+ = 15$) exceeded those obtained from the experimental data over the range $\lambda_x/R < 1$. The differences were negligible at long wavelengths. Large discrepancies at short wavelengths may have arisen from the resolution of hot-wires ($l^+ = 22$–30), i.e., an underestimate of the small-scale energy.[26,27] Away from the wall ($y^+ = 70$), the experimental data began to show the bimodal distribution, even though the magnitude of the distribution was small for $\lambda_x/R < 0.2$ and large for $\lambda_x/R > 1$, as compared with the magnitude of the distribution obtained in the present DNS. The present profile obtained at $y^+ = 213$ agreed
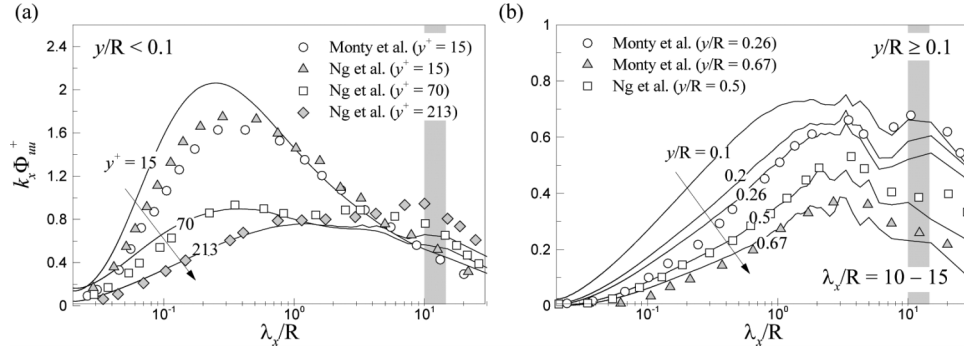
FIG. 7. 1-D pre-multiplied streamwise energy spectra of the streamwise velocity fluctuations at (a) $y/R < 0.1$ and (b) $y/R \geq 0.1$. The grey band represents the wavelength range $10 < \lambda_x/R < 15$.

well with the experimental data over short wavelengths, $\lambda_x/R < 1$, but trailed off at long wavelengths, $\lambda_x/R > 2$. In the outer region ($y/R \geq 0.1$) shown in Fig. 7(b), the spectra obtained here at wavelengths of $\lambda_x/R < 3$ resembled those obtained from the experimental data; however, the long wavelength energy intensities at wavelengths of $\lambda_x/R > 3$ were smaller than those obtained experimentally. The energy difference at long wavelengths decreased as y/R increased, e.g., $y/R = 0.67$.

Del Álamo and Jiménez[18] demonstrated that the energy spectra obtained using Taylor's hypothesis represent an artificially amplified long wavelength peak. The convection velocity was required to employ Taylor's hypothesis; however, the mean velocity was typically used for convenience. The difference between the convection velocity and the mean velocity became significant near the wall.[32] Because the large-scale structures were less energetic near the wall, the energy of the large-scale structures was not overestimated near the wall. At $y^+ = 70$, the influence of the spatial resolution was limited to the region associated with the small-scale structures. The large-scale structures became significant as the wall-normal distance increased,[13] i.e., the direct effects of Taylor's hypothesis were limited to wavelengths of $\lambda_x/R > 1$.[25] Away from the wall ($y/R = 0.67$), the overestimates of the large-scale structures diminished because the population of large-scale structures decreased due to spatial limitations in the core region of the pipe flow.[30] It is worth mentioning that although the exact convection velocity was applied to Taylor's hypothesis, it was difficult to describe both the spatial and temporal variations of the turbulent flows.[25,33]

Fig. 8 shows the 1-D $k_x \Phi_{uu}^+$ in $y/R \leq 0.1$ along the outer and inner coordinates (λ_x/R and λ_x/y). For comparison, the DNS channel data ($Re_\tau = 2003$ and 5186) of Hoyas and Jiménez[4] and Lee and Moser[5] were included. Fig. 8(a) shows that the profiles at $y^+ = 90$–300 agreed well over the wavelengths $\lambda_x/R = 2$–5, creating a plateau. Each profile along the inner coordinate shown in Fig. 8(b) also formed a plateau at $\lambda_x/y = 18$–160, even though the profiles did not overlap across
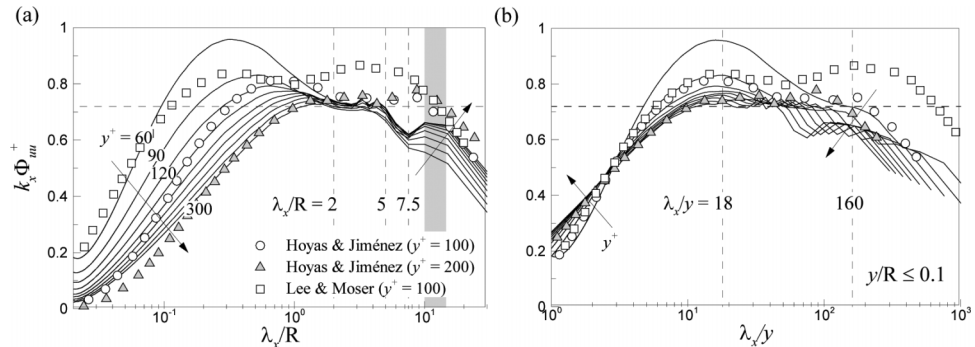

FIG. 8. 1-D pre-multiplied streamwise spectra of the streamwise velocity fluctuations at $y/R \leq 0.1$ along the (a) outer and (b) inner coordinates. y^+ increased with the interval of $\Delta y^+ = 30$. The grey band represents the wavelength range $10 < \lambda_x/R < 15$.

the wavelength domain. For example, the curve at $y^+ = 90$ induced a plateau for $\lambda_x/y = 70$–160, and the curve at $y^+ = 300$ induced a plateau for $\lambda_x/y = 18$–50, indicating that the energy plateau formed as a result of the structures with a streamwise size of $\lambda_x/R \approx 2$–5 at $y^+ = 90$ and 300. These flat regions correspond to the k_x^{-1} region.[17,20,21] Nickels *et al.*[21] observed the k_x^{-1} region for $\lambda_x/\delta \leq 0.1\pi$ and $\lambda_x/y \geq 5\pi$ at $y^+ \geq 100$ in the TBL ($Re_\tau = 14\,380$). Rosenberg *et al.*[17] found the k_x^{-1} region for $\lambda_x/R \leq 1\pi$ and $\lambda_x/y \geq 5\pi$ at $y^+ \geq 100$ in a turbulent pipe flow ($Re_\tau = 3334$). The present inner coordinate range (λ_x/y) of the k_x^{-1} region ($\lambda_x/y = 18$–160) was similar to those observed in experiments, but the outer coordinate values (λ_x/R) of the region ($\lambda_x/R = 2$–5) slightly exceeded those obtained experimentally due to an overestimate of the peak intensities in their studies. At higher Reynolds numbers for a turbulent pipe flow ($Re_\tau > 20\,000$), however, the k_x^{-1} region was not observed at $y^+ \approx 400$; instead, it appeared at $y^+ \approx 100$.[17] The k_x^{-1} region is the evidence of the attached eddy hypothesis.[19,20] Attached eddies are energy-containing motions and are proportional in size to the distance between their centers and the wall, i.e., attached to the wall. Nickels *et al.*[34] revealed that the log law does not readily describe the mean velocity without employing the attached eddy hypothesis. However, the beginning and ending locations of the k_x^{-1} region, $y^+ = 90$ and 300, were similar to those obtained in the power law region in Fig. 3(a). A state in which both the k_x^{-1} region in the wavenumber space and the log law in the physical space were satisfied was termed the complete similarity.[19] Incomplete similarity,[22] on the other hand, was observed in the present turbulent pipe flow by demonstrating the applicability of a power law in the mean velocity at $y^+ \leq 300$. Because the mean velocity followed a power law, the viscous effects persisted in the physical overlap region, although the k_x^{-1} region appeared in the spectra.

   The bimodal distributions are shown in Figs. 7 and 8. The short wavelength spectral peak grew with increasing y^+ to $\lambda_x/R = 3$. A long wavelength spectral peak was observed for $\lambda_x/R = 10$–15 in Fig. 6, corresponding to the VLSMs colored by the grey band. Because the grid system employed here permitted streamwise wavelengths up to $30/n$ (n is an integer between 1 and $N_x/2$), the wavelengths of the VLSMs were only 15R, 10R, and so on, creating large variations in the long wavelengths shown in Fig. 7(b). Even though there were discrete gaps in the long wavelengths, the overall spectral shapes were not changed.[25] The bimodal distribution appeared in both the short and long wavelength spectral peaks. The peak at long wavelengths did not surpass the peak at short wavelengths. The long wavelength energy at $\lambda_x/R = 10$–15 increased as the wall-normal distance increased. A deep valley at $\lambda_x/R = 7.5$ in Fig. 8(a) was observed due to the sudden increase in the energy spectrum. The sudden increase was associated with VLSMs and was amplified at high Reynolds numbers. Note that this sudden increase was not observed in the low-Reynolds-number flows.[15,25] Although the Reynolds number ($Re_\tau = 2003$) employed in Chin *et al.*[3] was high enough to produce active VLSMs, the computational domain length was limited to $3\pi R$, and a long wavelength spectral peak may not have been observed.

   Fig. 9 shows a two-dimensional (2-D) contour map of $k_x \Phi_{uu}^+$. The inner and outer sites were located, respectively, at $y^+ = 13$ ($\lambda_x^+ = 800$) and $y/R = 0.087$ ($\lambda_x/R = 10$). The inner site was created by the self-sustaining near-wall cycle.[13] Note that the wavelength of the outer site ($\lambda_x/R = 10$) exceeded $\lambda_x/\delta = 6$ in the TBLs.[13] The presence of an outer site has been reported in many experiments as resulting from the activation of VLSMs.[11–13,17] This outer site was not identical to the outer peak in the streamwise turbulence intensity. The short wavelength spectral peaks along the wall-normal location were detected in the 1-D energy profile. The small-scale energy near the wall grew into the outer-layer large-scale energy in a linear fashion according to $\lambda_x/R = 20y/R$ (white dashed line). The linear growth of the structures was closely associated with the k_x^{-1} region denoted by the black solid box ($\lambda_x/R = 2 \sim 5$ and $y^+ = 90 \sim 300$). At low Reynolds numbers, the k_x^{-1} region did not exist.[3,15,25] As the Reynolds number increased, the linear growth of energy between the inner and outer regions became active and helped to form the k_x^{-1} region with $\lambda_x/R = 2$–5 (Fig. 9). On the other hand, the outer regions of the VLSMs were isolated from the energy of the SSMs and LSMs. As shown in Figs. 7(b) and 8(a), the energy of the VLSMs was shown at $\lambda_x/R = 10$–15 regardless of the wall-normal locations. This indicated that the VLSMs did not grow linearly with the wall-normal distance but existed with the fixed wavelengths, i.e., the VLSMs were not the attached eddies. In the energy sense, the SSMs and LSMs did not contribute to the formation of the VLSMs, and the VLSMs were autonomously generated.[35] Since the energy
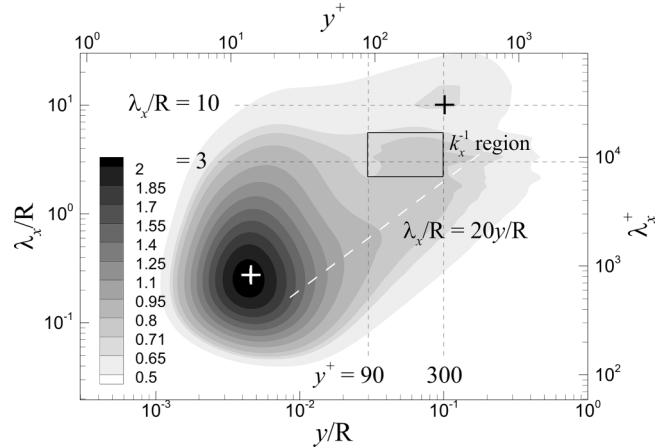
FIG. 9. 2-D contour of the pre-multiplied streamwise energy spectra corresponding to the streamwise velocity fluctuations. The black solid box indicates the k_x^{-1} region. The white dashed line indicates the linear growth of $\lambda_x/R = 20y/R$. The cross symbols represent the inner and outer sites at $y^+ = 13$ ($\lambda_x^+ = 800$) and $y/R = 0.087$ ($\lambda_x/R = 10$), respectively.

growth from the SSMs to the LSMs became populated with increasing the Reynolds number, this energy transfer produced a large population of the LSMs, and the generated adjacent LSMs resulted in the continuous concatenation along the streamwise direction, i.e., the VLSMs.[16,29,32,36] The high Reynolds number flow produced the isolated energy peak of the VLSMs at long wavelengths. As the Reynolds number increased further, the energy associated with the VLSMs increased even more significantly. The deep valley shown in Fig. 8 would be filled with the big VLSM energy at high Reynolds numbers. Note that the energy spectrum in a turbulent channel flow[5] was similar in shape to the spectrum suggested in our studies.

The pre-multiplied spanwise energy spectra of the streamwise velocity fluctuations ($k_z\Phi_{uu}^+$) are shown in Fig. 10. The bimodal distribution is shown in the 1-D plot. The short wavelength spectral peak grew up to $\lambda_z/R = 0.6$ with increasing the wall-normal location, and the long wavelength spectral peak arose at $\lambda_z/R = 1.4$–2. Two k_z^{-1} regions were observed at $y^+ = 3$ and 150 ($y/R = 0.05$).[19,20] The spanwise energy with $\lambda_z/R = 0.3$–0.6 in the overlap region ($y^+ = 150$) penetrated into the viscous sublayer ($y^+ \approx 3$). The existence of the k_z^{-1} region was consistent with the previous DNS studies of TBLs[37] and turbulent channel flow,[5,38] although the wall-normal locations were slightly different. In the 2-D contour map, the inner and outer sites were located at $y^+ = 12$ ($\lambda_z^+ = 113$)[39] and $y/R = 0.189$ ($\lambda_z/R = 1.3$), respectively. The spanwise outer site ($y/R = 0.189$) was located further away than the streamwise outer site ($y/R = 0.087$), implying
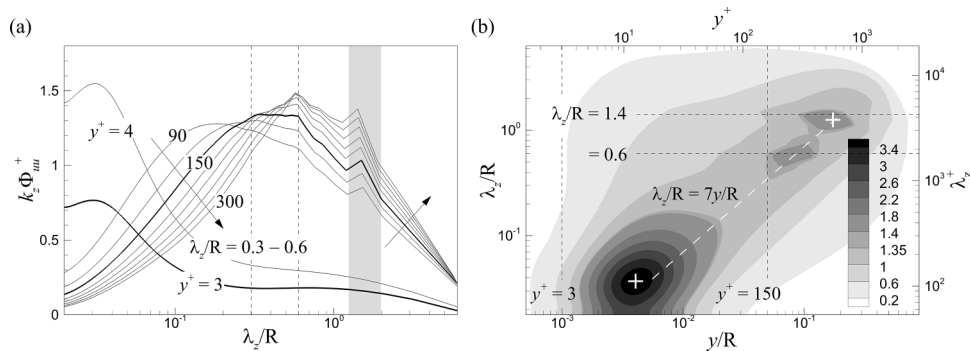

FIG. 10. The pre-multiplied spanwise energy spectra of the streamwise velocity fluctuations. (a) 1-D plots and (b) 2-D contour. The grey band represents the wavelength range $1.4 < \lambda_z/R < 2$. The cross symbols represent the inner and outer sites at $y^+ = 12$ ($\lambda_z^+ = 113$) and $y/R = 0.189$ ($\lambda_z/R = 1.3$), respectively. The white dashed line indicates the linear growth of $\lambda_z/R = 7y/R$.

that the VLSMs in the outer region maintained their energy along the spanwise direction stronger than the streamwise direction.[15,25] The small-scale energy near the wall developed into the large-scale energy in the outer region through a linear fashion $\lambda_z/R = 7y/R$ (white dashed line).

2. Energy spectra of the Reynolds shear stress

The pre-multiplied energy spectra of the Reynolds shear stresses ($k_x\Phi_{-uv}{}^+$) are plotted at $y/R \leq 0.1$ along the outer and inner coordinates in Figs. 11(a) and 11(b), respectively. In Fig. 11(b), the profiles in the region $y^+ = 210$–300 agreed well over the wavelengths $\lambda_x/R = 1$–3 and $\lambda_x/y = 1$–3 with the logarithmic inclination, i.e., the logarithmic correction of the $k_x{}^{-1}$ region.[40] This result indicated that the structures satisfying both the outer and inner coordinates were present in the Reynolds shear stress. In the outer region, $y/R \geq 0.1$ in Fig. 11(c), the profiles along the outer coordinate did not overlap across the wavelengths. Long wavelength peaks were observed at $\lambda_x/R = 10$–15 and $y/R = 0.1$–0.4, i.e., the bimodal distribution. Away from the wall, the short wavelength peaks became saturated at $\lambda_x/R = 2$.

The contour map shown in Fig. 11(d) shows the inner and outer sites at $y^+ = 30$ ($\lambda_x{}^+ = 710$) and $y/R = 0.173$ ($\lambda_x/R = 10$), respectively. The wavelength of the inner site was shorter than that of $k_x\Phi_{uu}{}^+$, and the wavelength of the outer site assumed the same value. The inner and outer sites were located further from the wall than those of $k_x\Phi_{uu}{}^+$. These characteristics arose from the wall-normal fluctuating structures, which became streamwise elongated in the outer region and subsequently detached.[25] The asymptotic line along the short wavelength peaks was linear, $\lambda_x/R = 10y/R$.[40] Turbulence structures grew from small- to large-scales along the line, although the structures grew at half the speed of the $k_x\Phi_{uu}{}^+$ structures. After the LSMs ($\lambda_x/R \geq 1$) had emerged, the LSM sizes converged to $\lambda_x/R = 2$ at $y/R \geq 0.2$. The size of each structure was proportional to the distance between the center and the wall. This did not necessarily mean that these structures were attached, however, because the $k_x{}^{-1}$ region was not observed in the energy spectra.[23] Instead, a logarithmic inclination was observed in the overlap region in Fig. 11(b).
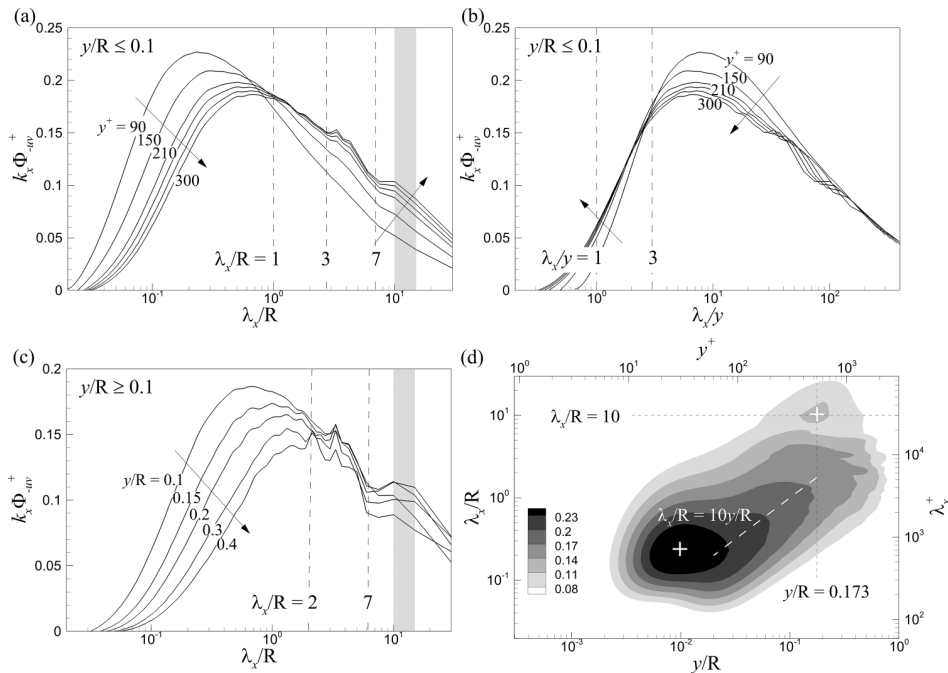

FIG. 11. The pre-multiplied streamwise energy spectra of the Reynolds shear stress. 1-D plots normalized by the friction velocity along the (a) outer and (b) inner coordinates in $y/R \leq 0.1$ and (c) along the outer coordinate in $y/R \geq 0.1$. (d) 2-D contour. The grey bands in (a) and (c) depict the wavelength range $10 < \lambda_x/R < 15$. The white dashed line indicates the linear growth of $\lambda_x/R = 10y/R$. The cross symbols represent the inner and outer positions at $y^+ = 30$ ($\lambda_x{}^+ = 710$) and $y/R = 0.173$ ($\lambda_x/R = 10$).
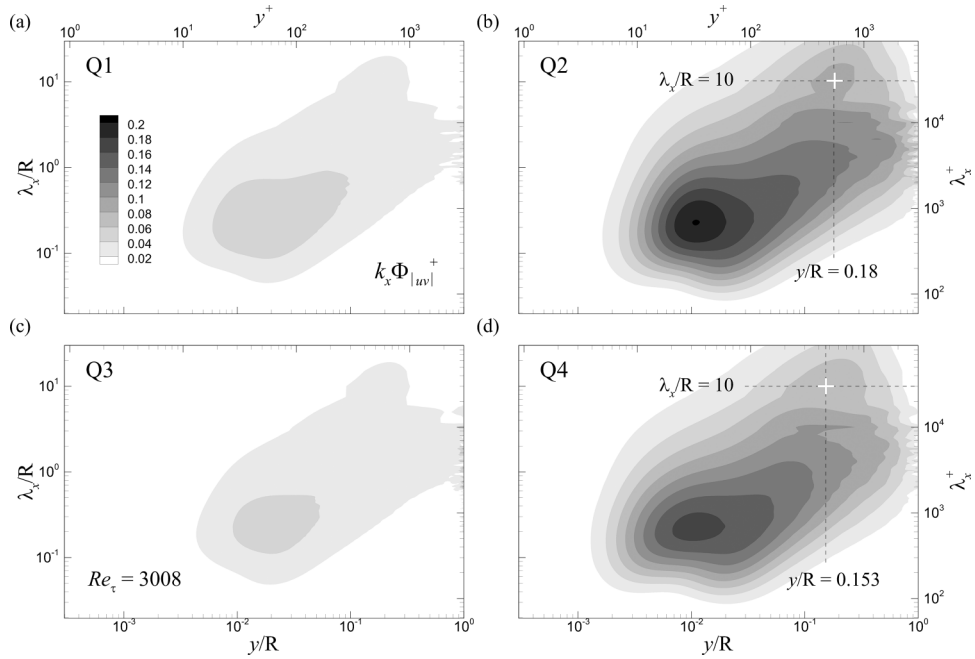
FIG. 12. 2-D pre-multiplied streamwise energy spectra of the quadrants. (a) Q1, (b) Q2, (c) Q3, and (d) Q4.

The Reynolds shear stress is divided into four quadrants of the energy spectrum in Fig. 12. The quadrant spectra were obtained by the multiplication of the energy spectra with the weight values, which were the fractions of the quadrants against the Reynolds shear stress,

$$k_x \Phi^+ \big|_{Qi} = \frac{\langle u'v'|Qi \rangle}{\langle u'v' \rangle} k_x \Phi_{uv}^+ \, , \quad i = 1, 2, 3, 4. \tag{6}$$

The energy spectra of the Q2 event ($\langle u' < 0 \, \& \, v' > 0 \rangle$) and the Q4 event ($\langle u' > 0 \, \& \, v' < 0 \rangle$) created strong inner and outer sites, whereas the energy spectra of the Q1 event ($\langle u' > 0 \, \& \, v' > 0 \rangle$) and the Q3 event ($\langle u' < 0 \, \& \, v' < 0 \rangle$) were small. The energy spectra of the Q1 and Q3 events were spread along the diagonal, indicating that the Q1 and Q3 events with short and long wavelengths were locally effective near the wall and in the outer region, respectively. The relatively strong energy of the Q1 event near the wall indicated that the small-scale structures near the wall played an important role in generating the outward motions of the high-speed flow. The energy spectra of the Q2 and Q4 events covered a greater area than the Q1 and Q3 events. In particular, the long wavelength energy of the Q2 and Q4 events deeply penetrated the vicinity of the wall ($y^+ \approx 10$), which was not observed in $k_x \Phi_{-uv}^+$. These results suggested that elongated sweep and ejection motions created a footprint near the wall, even though their energy was weak.[13] The energy spectra of the Q2 and Q4 events encompassed the outer sites located at $y/R = 0.18$ ($\lambda_x/R = 10$) and $y/R = 0.153$ ($\lambda_x/R = 10$), respectively. The low-speed flow with an outward motion (ejection) was further located than the high-speed flow with an inward motion (sweep) in the outer region. Both events simultaneously affected the outer energy in the Reynolds shear stress because the outer site of the Reynolds shear stress shown in Fig. 11(d) was located between the outer sites of the Q2 and Q4 events. The energy of the Q4 event was stronger than that of the Q2 event very near the wall ($y^+ < 15$), and vice versa above $y^+ = 15$ ($y^+ > 15$). The Q2 event (ejection) pushed the structures to the outer region, and the Q4 event (sweep) pulled the structures inward toward the wall.

IV. CONCLUSIONS

A DNS of turbulent pipe flows was performed at a high Reynolds number, $Re_\tau = 3008$. The streamwise mean velocity was found to follow the power law ($y^+ = 90$–300; $y/R = 0.03$–0.1) in

the inertial layer, as validated by the indicator function. The scale separation of the Reynolds shear stress revealed that the contributions of the SSMs were independent of the Reynolds numbers. The LSMs were more responsible for the constant-stress layer in the Reynolds shear stress than the SSMs. The LSMs contributed more to the growth of the mean velocity in the overlap region than the SSMs. Because the LSMs were more populated in the channel flow than in the pipe flow, more active LSMs in the channel flow contributed to the log law in the mean velocity more strongly than they did in the pipe flow. The pre-multiplied streamwise spectra of the streamwise velocity fluctuations revealed the k_x^{-1} region for $\lambda_x/R = 2$–5 and $\lambda_x/y = 18$–160 at $y^+ = 90$–300, which was the same wall-normal region of the power law. The existence of the k_x^{-1} region supported the attached eddy hypothesis. The linear growth of $\lambda_x/R = 20y/R$, from small-scale energy to large-scale energy developed attached eddies, which formed the k_x^{-1} region, i.e., increased the energy of the LSMs. VLSMs were formed due to the streamwise concatenation of LSMs, and the bimodal distribution with short and long wavelength peaks was observed. The streamwise inner and outer sites were observed at $y^+ = 13$ ($\lambda_x^+ = 800$) and $y/R = 0.087$ ($\lambda_x/R = 10$), respectively. The k_z^{-1} region was observed with the bimodal distribution. The k_z^{-1} region for $\lambda_z/R = 0.3$–0.6 was located at $y^+ = 3$ and 150. The spanwise inner and outer sites at $y^+ = 12$ ($\lambda_z^+ = 113$) and $y/R = 0.189$ ($\lambda_z/R = 1.3$) were connected by the linear growth $\lambda_z/R = 7y/R$. The bimodal distribution was also observed in the pre-multiplied streamwise spectra of the Reynolds shear stress. Although the SSMs near the wall grew linearly to form LSMs by $\lambda_x/R = 10y/R$, those structures were not attached due to the absence of the k_x^{-1} region. The inner and outer sites were located at $y^+ = 30$ ($\lambda_x^+ = 710$) and $y/R = 0.173$ ($\lambda_x/R = 10$), and the locations shifted further away from the wall due to the wall-normal fluctuating structures. The outer site was formed by the large outer structures of the Q2 and Q4 events. The elongated structures of the Q2 and Q4 events penetrated into the near-wall region as a footprint.

ACKNOWLEDGMENTS

[1] M. Hultmark, M. Vallikivi, S. C. C. Bailey, and A. J. Smits, "Logarithmic scaling of turbulence in smooth- and rough-wall pipe flow," J. Fluid Mech. **728**, 376–395 (2013).

[2] X. Wu and P. Moin, "A direct numerical simulation study on the mean velocity characteristics in turbulent pipe flow," J. Fluid Mech. **608**, 81–112 (2008).

[3] C. Chin, J. P. Monty, and A. Ooi, "Reynolds number effects in DNS of pipe flow and comparison with channels and boundary layers," Int. J. Heat Fluid Flow **45**, 33–40 (2014).

[4] S. Hoyas and J. Jiménez, "Scaling of the velocity fluctuations in turbulent channels up to $Re_\tau = 2003$," Phys. Fluids **18**, 011702 (2006).

[5] M. Lee and R. D. Moser, "Direct numerical simulation of turbulent channel flow up to $Re \approx 5200$," J. Fluid Mech. **774**, 395–415 (2015).

[6] J. P. Monty, J. A. Stewart, R. C. Williams, and M. S. Chong, "Large-scale features in turbulent pipe and channel flows," J. Fluid Mech. **589**, 147–156 (2007).

[7] J. H. Lee and H. J. Sung, "Comparison of very-large-scale motions of turbulent pipe and boundary layer simulations," Phys. Fluids **25**, 045103 (2013).

[8] H. M. Nagib and K. A. Chauhan, "Variations of von Kármán coefficient in canonical flows," Phys. Fluids **20**, 101518 (2008).

[9] I. Marusic, J. P. Monty, M. Hultmark, and A. J. Smits, "On the logarithmic region in wall turbulence," J. Fluid Mech. **716**, R3 (2013).

[10] B. J. McKeon, J. Li, W. Jiang, J. F. Morrison, and A. J. Smits, "Further observations on the mean velocity distribution in fully developed pipe flow," J. Fluid Mech. **501**, 135–147 (2004).

[11] J. P. Monty, N. Hutchins, H. C. H. Ng, I. Marusic, and M. S. Chong, "A comparison of turbulent pipe, channel, and boundary layer flows," J. Fluid Mech. **632**, 431–442 (2009).

[12] H. C. H. Ng, J. P. Monty, N. Hutchins, M. S. Chong, and I. Marusic, "Comparison of turbulent channel and pipe flows with varying Reynolds number," Exp. Fluids **51**, 1261–1281 (2011).

[13] N. Hutchins and I. Marusic, "Evidence of very long meandering features in the logarithmic region of turbulent boundary layers," J. Fluid Mech. **579**, 1–28 (2007).

[14] R. Mathis, N. Hutchins, and I. Marusic, "Large-scale amplitude modulation of the small-scale structures in turbulent boundary layers," J. Fluid Mech. **628**, 311–337 (2009).

[15] J. Ahn, J. H. Lee, S. J. Jang, and H. J. Sung, "Direct numerical simulations of fully developed turbulent pipe flows for $Re_\tau = 180$, 544, and 934," Int. J. Heat Fluid Flow **44**, 222–228 (2013).

[16] K. C. Kim and R. J. Adrian, "Very large-scale motion in the outer layer," Phys. Fluids **11**, 417–422 (1999).

[17] B. J. Rosenberg, M. Hultmark, M. Vallikivi, S. C. C. Bailey, and A. J. Smits, "Turbulence spectra in smooth- and rough-wall pipe flow at extreme Reynolds numbers," J. Fluid Mech. **731**, 46–63 (2013).

[18] J. C. del Álamo and J. Jiménez, "Estimation of turbulent convection velocities and correlations to Taylor's approximation," J. Fluid Mech. **640**, 5–26 (2009).

[19] A. A. Townsend, *The Structure of Turbulent Shear Flow*, 2nd ed. (Cambridge University Press, 1976).

[20] A. E. Perry, S. Henbest, and M. S. Chong, "A theoretical and experimental study of wall turbulence," J. Fluid Mech. **165**, 163–199 (1986).

[21] T. B. Nickels, I. Marusic, S. Hafez, and M. S. Chong, "Evidence of the k_l^{-1} law in a high-Reynolds-number turbulent boundary layer," Phys. Rev. Lett. **95**, 074501 (2005).

[22] J. F. Morrison, B. J. McKeon, W. Jiang, and A. J. Smits, "Scaling of the streamwise velocity component in turbulent pipe flow," J. Fluid Mech. **508**, 99–131 (2004).

[23] J. Jiménez, "Near-wall turbulence," Phys. Fluids **25**, 101302 (2013).

[24] K. Kim, S. J. Baek, and H. J. Sung, "An implicit velocity decoupling procedure for the incompressible Navier–Stokes equations," Int. J. Numer. Methods Fluids **38**(2), 125–138 (2002).

[25] X. Wu, J. R. Baltzer, and R. J. Adrian, "Direct numerical simulation of a 30R long turbulent pipe flow at R$^+$ = 685: Large- and very-large-scale motions," J. Fluid Mech. **698**, 235–281 (2012).

[26] N. Hutchins, T. B. Nickels, I. Marusic, and M. S. Chong, "Hot-wire spatial resolution issues in wall-bounded turbulence," J. Fluid Mech. **635**, 103–136 (2009).

[27] C. Chin, N. Hutchins, A. Ooi, and I. Marusic, "Spatial resolution correction for hot-wire anemometry in wall turbulence," Exp. Fluids **50**, 1443–1453 (2011).

[28] C. Chin, J. Philip, J. Klewicki, A. Ooi, and I. Marusic, "Reynolds-number-dependent turbulent inertia and onset of log region in pipe flows," J. Fluid Mech. **757**, 747–769 (2014).

[29] J. Lee, J. H. Lee, J.-I. Choi, and H. J. Sung, "Spatial organization of large-and very-large-scale motions in a turbulent channel flow," J. Fluid Mech. **749**, 818–840 (2014).

[30] J. Lee, J. Ahn, and H. J. Sung, "Comparison of large- and very-large-scale motions in turbulent pipe and channel flows," Phys. Fluids **27**, 025101 (2015).

[31] B. J. McKeon and K. R. Sreenivasan, "Introduction: Scaling and structure in high Reynolds number wall-bounded flows," Philos. Trans. R. Soc., A **365**, 635–646 (2007).

[32] J. H. Lee and H. J. Sung, "Very-large-scale motions in a turbulent boundary layer," J. Fluid Mech. **673**, 80–120 (2011).

[33] D. J. C. Dennis and T. B. Nickels, "On the limitations of Taylor's hypothesis in constructing long structures in a turbulent boundary layer," J. Fluid Mech. **614**, 197–206 (2008).

[34] T. B. Nickels, I. Marusic, S. Hafez, N. Hutchins, and M. S. Chong, "Some predictions of the attached eddy model for a high Reynolds number boundary layer," Philos. Trans. R. Soc., A **365**, 807–822 (2007).

[35] J. C. del Álamo, J. Jiménez, P. Zandonade, and R. D. Moser, "Self-similar vortex clusters in the turbulent logarithmic region," J. Fluid Mech. **561**, 329–358 (2006).

[36] J. R. Baltzer, R. J. Adrian, and X. Wu, "Structural organization of large and very large scales in turbulent pipe flow simulation," J. Fluid Mech. **720**, 236–279 (2013).

[37] S. Pirozzoli and M. Bernardini, "Probing high-Reynolds-number effects in numerical boundary layers," Phys. Fluids **25**, 021704 (2013).

[38] M. Bernardini, S. Pirozzoli, and P. Orlandi, "Velocity statistics in turbulent channel flow up to Re_τ = 4000," J. Fluid Mech. **742**, 171–191 (2014).

[39] J. M. Hamilton, J. Kim, and F. Waleffe, "Regeneration mechanisms of near-wall turbulent structures," J. Fluid Mech. **287**, 317–348 (1995).

[40] J. C. del Álamo, J. Jiménez, P. Zandonade, and R. D. Moser, "Scaling of the energy spectra of turbulent channels," J. Fluid Mech. **500**, 135–144 (2004).